


## Article

# Cell-Membrane Biomimetic Indocyanine Green Liposomes for Phototheranostics of Echinococcosis

Xinxin Xiong<sup>1</sup>, Jun Li<sup>1</sup>, Duyang Gao<sup>2</sup>, Zonghai Sheng<sup>2</sup> , Hairong Zheng<sup>2</sup> and Wenya Liu<sup>1,\*</sup>

<sup>1</sup> The First Affiliated Hospital of Xinjiang Medical University, Urumqi 830011, China; 13095025355@163.com (X.X.); lijun@xjmu.edu.cn (J.L.)

<sup>2</sup> Paul C. Lauterbur Research Center for Biomedical Imaging, Institute of Biomedical and Health Engineering, Shenzhen Institute of Advanced Technology, Chinese Academy of Sciences, Shenzhen 518055, China; dy.gao@siat.ac.cn (D.G.); zh.sheng@siat.ac.cn (Z.S.); hr.zheng@siat.ac.cn (H.Z.)

\* Correspondence: wenyaliu2022@xjmu.edu.cn

**Abstract:** Echinococcosis is an important zoonotic infectious disease that seriously affects human health. Conventional diagnosis of echinococcosis relies on the application of large-scale imaging equipment, which is difficult to promote in remote areas. Meanwhile, surgery and chemotherapy for echinococcosis can cause serious trauma and side effects. Thus, the development of simple and effective treatment strategies is of great significance for the diagnosis and treatment of echinococcosis. Herein, we designed a phototheranostic system utilizing neutrophil-membrane-camouflaged indocyanine green liposomes (Lipo-ICG) for active targeting the near-infrared fluorescence diagnosis and photothermal therapy of echinococcosis. The biomimetic Lipo-ICG exhibits a remarkable photo-to-heat converting performance and desirable active-targeting features by the inflammatory chemotaxis of the neutrophil membrane. In-vitro and in-vivo studies reveal that biomimetic Lipo-ICG with high biocompatibility can achieve in-vivo near-infrared fluorescence imaging and phototherapy of echinococcosis in mouse models. Our research is the first to apply bionanomaterials to the phototherapy of echinococcosis, which provides a new standard for the convenient and noninvasive detection and treatment of zoonotic diseases.

**Keywords:** fluorescence imaging; photothermal therapy; indocyanine green; cell-membrane biomimetic engineering; echinococcosis



**Citation:** Xiong, X.; Li, J.; Gao, D.; Sheng, Z.; Zheng, H.; Liu, W. Cell-Membrane Biomimetic Indocyanine Green Liposomes for Phototheranostics of Echinococcosis. *Biosensors* **2022**, *12*, 311. <https://doi.org/10.3390/bios12050311>

Received: 10 April 2022

Accepted: 6 May 2022

Published: 9 May 2022

**Publisher's Note:** MDPI stays neutral with regard to jurisdictional claims in published maps and institutional affiliations.



**Copyright:** © 2022 by the authors. Licensee MDPI, Basel, Switzerland. This article is an open access article distributed under the terms and conditions of the Creative Commons Attribution (CC BY) license (<https://creativecommons.org/licenses/by/4.0/>).

## 1. Introduction

Echinococcosis, also known as hydatid disease, is a serious infectious disease caused by the larval stages of cestodes of the genus *echinococcus* [1–3]. *Echinococcus* is an important zoonotic infectious disease that can be widely spread among host dogs, intermediate host sheep and cattle, and humans, and which is seriously affecting human health and livestock production [4–6]. Currently, conventional medical imaging techniques, including chest radiography [7], X-ray computed tomography [8], magnetic resonance imaging [9], and ultrasound imaging [10], have been applied for the clinical diagnosis of echinococcosis. Surgery and medication are adopted as the main methods to treat echinococcosis [11–13]. Nevertheless, it is difficult to perform advanced imaging procedures to diagnose and evaluate therapeutic efficacy in remote pastoral areas [14]. Furthermore, surgical trauma and serious side effects of medications also hinder their widespread applications [15]. Therefore, there is an urgent need to design convenient, noninvasive and efficient methods for the theranostics of echinococcosis.

Phototheranostics is a hybrid technology that utilizes small molecule probes or nanoprobes for optical molecular imaging-guided phototherapy for a variety of diseases, including cancer [16–18], bacterial infections [19], and neurodegenerative diseases [20]. Compared with traditional medical imaging and treatment methods, it has unique advantages such as high sensitivity, good selectivity, and non-invasiveness [21–25]. Currently, a

variety of phototheranostic agents, such as indocyanine green (ICG) [26], polymer dots [27], carbon nanotubes [28], graphene [29], gold nanorods [30], etc. [31], have been developed for high-performance phototheranostics. Among these materials, only ICG is clinically used as the U.S. Food and Drug Administration-approved agent [32–34], offering great potential for phototheranostics of zoonotic diseases. Nevertheless, ICG suffers from short blood half-life, low stability, and a non-active targeting ability, which hinders its application in hydatid disease [35–38].

Herein, we report the use of neutrophil-membrane camouflaged ICG liposomes (Neu-lipo-ICG) for active targeting the phototheranostics of echinococcosis in a mouse model. Liver tissues infected with hydatid disease may produce severe inflammation, which accumulates a large number of neutrophils due to their inflammatory chemotaxis [35]. Inspired by unique characteristics, we prepared Neu-lipo-ICG using neutrophil-membrane camouflage technology to enhance its active targeting for the precise photodiagnosis and phototherapy of echinococcosis. Neu-lipo-ICG shows bright near-infrared fluorescence and a good photothermal performance. Importantly, it enables the performance of in-vivo fluorescence imaging to visualize echinococcosis lesions with a high signal-to-background ratio, and photothermal therapy under near-infrared laser irradiation. Our results provide a novel paradigm for the accurate diagnosis and effective treatment of echinococcosis.

## 2. Materials and Methods

First, 1,2-dioleoyl-sn-glycero-3-phosphocholine (DOPC) and 1,2-distearoyl-sn-glycero-3-phosphoethanolamine-N-[amino(polyethylene glycol)-2000] (DSPE-PEG<sub>2000</sub>) were purchased from Avanti (Alabaster, Birmingham, AL, USA). ICG was obtained from Sigma-Aldrich (St Louis, MO, USA). Fetal bovine serum (FBS) and Trypsin ethylenediaminetetraacetic acid (EDTA) were from Gibco Life Technologies (Grand Island, NY, USA).

### Preparation and characterization of Neu-lipo-ICG

Lipo-ICG was prepared through a thin-film strategy. Briefly, DOPC and DSPE-PEG<sub>2000</sub> with a molar ratio of 95/5 were dissolved in the CHCl<sub>3</sub> and formed a thin film by being evaporated with nitrogen and dried in a vacuum for 4 h. The dry film was then rehydrated by adding PBS containing an adequate amount of ICG. The mixture was further subjected to freeze–thaw for 5 cycles using liquid nitrogen and 65 °C water bath, which was further extruded through a polycarbonate membrane with a pore diameter of 100 nm 15 times.

The improved Percoll gradient method was used to isolate peripheral blood neutrophils from fresh whole blood of mice. Briefly, after centrifugation purification and re-suspension in phosphate-buffered saline (PBS) containing ethylenediaminetetraacetic acid (EDTA), samples were carefully placed on a three-layer gradient in PBS diluted with 78%, 69%, and 52% Percoll. Neutrophils were collected from the 69–78% interface and the upper 78% layer by centrifugation at 800 × *g* at 21 °C for 30 min in a test tube.

To obtain neutrophils, the sample was gently suspended in a cold, hypotonic solution buffer with a cocktail of protease inhibitors. After 15 min of incubation in an ice bath, homogenization was performed 50 times with a Dounce homogenizer and a tightly mounted pestle. The homogenate was centrifuged at 700 × *g* at 4 °C for 10 min to remove unbroken cells and nuclei. The neutrophil membrane was collected and centrifuged at 14,000 × *g* for 30 min at 4 °C.

Neu-lipo-ICG was prepared with continuous extrusion and freezing treatments of Lipo-ICG and neutrophil membrane derived from activated neutrophils in mouse peripheral blood.

The purified Lipo-ICG and Neu-lipo-ICG solution were obtained by removal of the free ICG molecules through dialyzing (7 KD, 48 h). The encapsulation efficiency of the Lipo-ICG and Neu-lipo-ICG was further measured by the equation:

$$\text{Encapsulation efficiency (\%)} = \frac{\text{Mass of ICG in product}}{\text{Total mass of ICG}} \times 100$$

#### Mouse models infected with alveolar echinococcosis

The animal experiments were approved by the Ethics Committee of Xinjiang Medical University. C57 mice (female,  $20 \pm 5$  g, age of 8–10 weeks) were anesthetized with 10% chloral hydrate solution by intraperitoneal injection. We further injected protoscoleces (200–300  $\mu\text{L}$ ) into liver tissue through a routine procedure. Two months after these procedures, the mouse models were evaluated by ultrasound and magnetic resonance imaging.

#### Separating protoscoleces from liver tissue in mouse models

The mice infected with alveolus echinococcosis were euthanized, and their liver tissue was taken out by laparotomy. The obtained samples were cut into pieces and ground to form tissue homogenates. After filtration to remove necrotic tissue and erythrocytes, highly active protoscoleces were obtained with a concentration of 20% ( $2.0 \times 10^4$  protoscoleces  $\text{mL}^{-1}$ ).

#### In-vivo near-infrared fluorescence imaging

Neu-lipo-ICG or Lipo-ICG (dose =  $0.5 \text{ mg Kg}^{-1}$ ) was administrated into mice infected with alveolus echinococcosis through tail-vein injection, and near-infrared fluorescent signals were detected at various time points (1, 3, 6, 12 and 24 h) using the commercial fluorescence imaging system (IVIS Spectrum, PerkinElmer, Waltham, MA, USA).

#### In-vivo photothermal therapy

The mice models of echinococcosis were intravenously injected with Lipo-ICG and Neu-lipo-ICG (dose =  $0.5 \text{ mg Kg}^{-1}$ ), respectively. After 24 h post-injection, near-infrared laser (808 nm) irradiation in liver tissue was performed for 10 min ( $0.6 \text{ W cm}^{-2}$ ), and temperature variation was monitored by an infrared thermal camera (FLIR A300, Wilsonville, OR, USA). The photothermal efficacy was assessed by ultrasound (ACUSON Sequoia512, 8–12 MHz probes) and magnetic resonance imaging (GE3.0T Signa EXCITE T1WI).

### 3. Results

#### 3.1. Synthesis and Characterization of Neu-Lipo-ICG

Neu-lipo-ICG was fabricated via continuous extrusion and freezing treatments of the Lipo-ICG and neutrophil membrane derived from activated neutrophils in mouse blood (Figure 1a). After the mechanical process, we conducted extensive physical and optical characterization of Neu-lipo-ICG. Transmission electron microscopy (TEM) images of negatively stained samples showed that Lipo-ICG and Neu-lipo-ICG exhibited an approximately spherical morphology with uniform size (Figure 1b,c). After the cell membrane camouflaging treatment, the particle size of Lipo-ICG decreased from  $\sim 128$  nm to  $\sim 119$  nm (Figure 1d); meanwhile, a coronal structure appeared in the shell layers of Lipo-ICG. It suggested that the neutrophil membrane was successfully modified onto the surface of Lipo-ICG by the extrusion and freezing treatments. The polydispersity index (PDI) of the Lipo-ICG and Neu-lipo-ICG was 0.126 and 0.098, respectively, indicating the nanoparticles possessed uniform size. Subsequently, the optical features of Neu-lipo-ICG were measured with absorption and emission spectra (Figure 1e,f). The results verified no obvious changes in the absorption and fluorescent emission peaks of Neu-lipo-ICG, correlating well with Lipo-ICG. The storage stabilities of Neu-lipo-ICG and the free ICG were evaluated by recording the fluorescence intensity under ambient condition ( $25^\circ\text{C}$ , dark), respectively. The obtained Neu-lipo-ICG showed a higher storage stability as compared with free ICG under the same conditions (Figure 1g). In addition, the encapsulation efficiency of Lipo-ICG and Neu-Lipo-ICG were calculated to be 84.2% and 83.5%, respectively. Consequently, as revealed by

the optical measurements, we speculated that Neu-lipo-ICG was competent for the fluorescence imaging of echinococcosis.

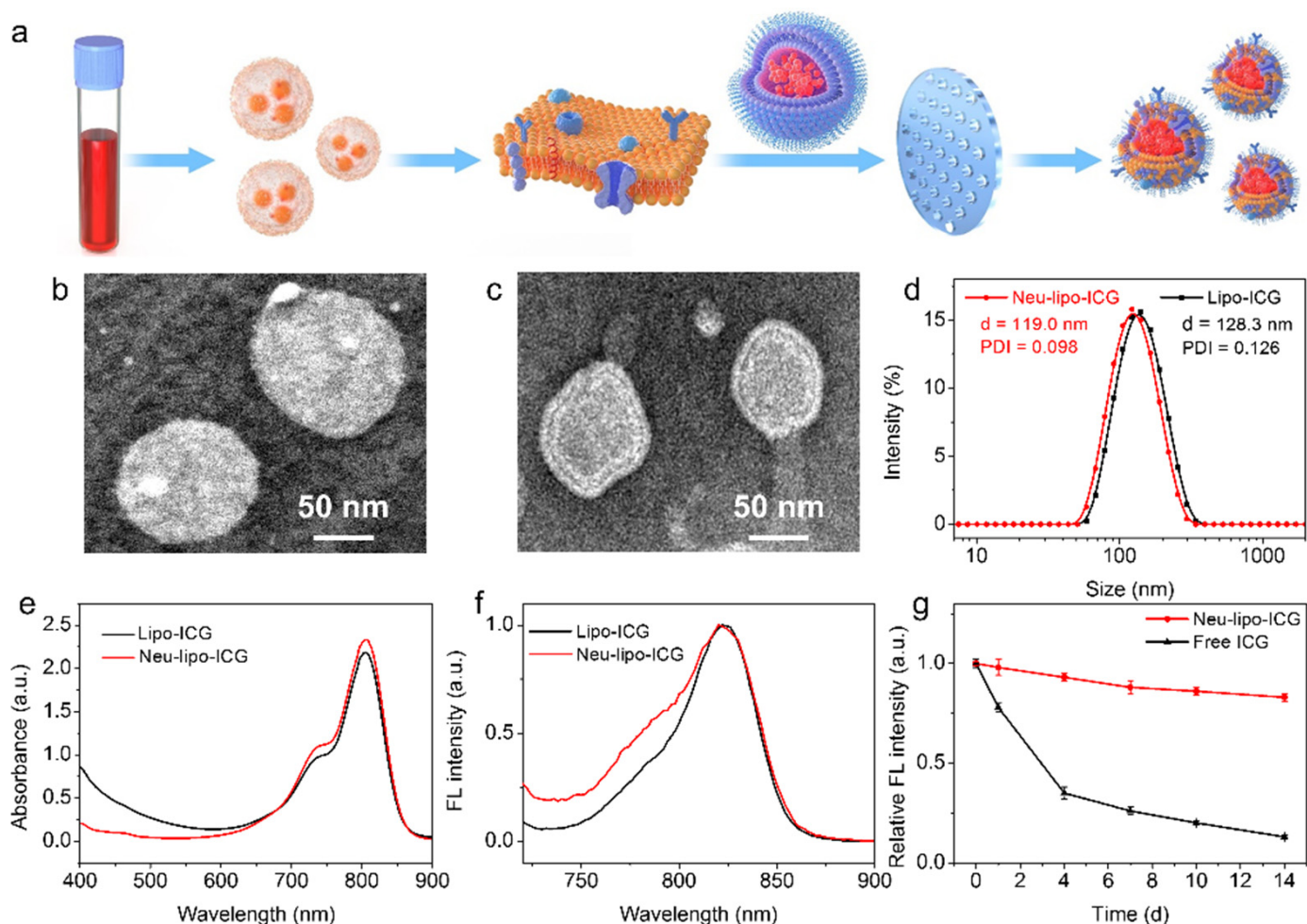


**Figure 1.** Synthesis of Neu-lipo-ICG. (a) Schematic representation of neutrophil membrane camouflaging Lipo-ICG. TEM images of Lipo-ICG (b) and Neu-lipo-ICG (c). (d) DLS measurements of Lipo-ICG and Neu-lipo-ICG. Absorption spectra (e) and emission fluorescence spectra (f) of Lipo-ICG and Neu-lipo-ICG (excitation: 710 nm). (g) Fluorescence varies of Neu-lipo-ICG and free ICG over storage (25 °C, dark).

### 3.2. In-Vitro Photothermal Performance of Neu-Lipo-ICG

Inspired by strong optical absorption in the near-infrared window, we investigated the photothermal performance of Neu-lipo-ICG under 808 nm laser exposure. There was a notable temperature increase in Neu-lipo-ICG at different concentrations, ranging from  $0 \mu\text{g mL}^{-1}$  to  $50 \mu\text{g mL}^{-1}$  (Figure 2a). The temperature of the Neu-lipo-ICG solution could reach  $45^\circ\text{C}$  for hyperthermia under 808 nm laser irradiation ( $0.6 \text{ W cm}^{-2}$ ,  $50 \mu\text{g mL}^{-1}$ ) for 5 min. Nevertheless, a negligible temperature increment was detected for a phosphate buffer solution (PBS) under the same experimental conditions. Additionally, the temperature of the Neu-lipo-ICG solution increased with laser density elevation from  $0.4 \text{ W cm}^{-2}$  to  $0.6 \text{ W cm}^{-2}$  (Figure 2b). The dose-dependent, irradiation-duration-dependent and laser-density-dependent features enabled Neu-lipo-ICG to be an efficient photo-to-heat converting agent for photothermal therapy. Given the favorable photothermal performance of Neu-lipo-ICG, we then evaluated its photothermal-treatment efficacy against hydatid larva separated from the liver tissue in mouse models. Morphological changes in hydatids were observed by a bright-field microscope. Neu-lipo-ICG did not induce morphological changes in hydatids after incubation for 2 h (Figure 2c), indicating

its good biocompatibility. In contrast, hydatids incubated with Neu-lipo-ICG were thermally destroyed under near-infrared laser exposure ( $0.6 \text{ W cm}^{-2}$ , 10 min) (Figure 2d), indicating a reduced size, missing surface hooks, and destroyed internal structures. The above results suggested a prominent photothermal effect of Neu-lipo-ICG that promoted hydatids' death.

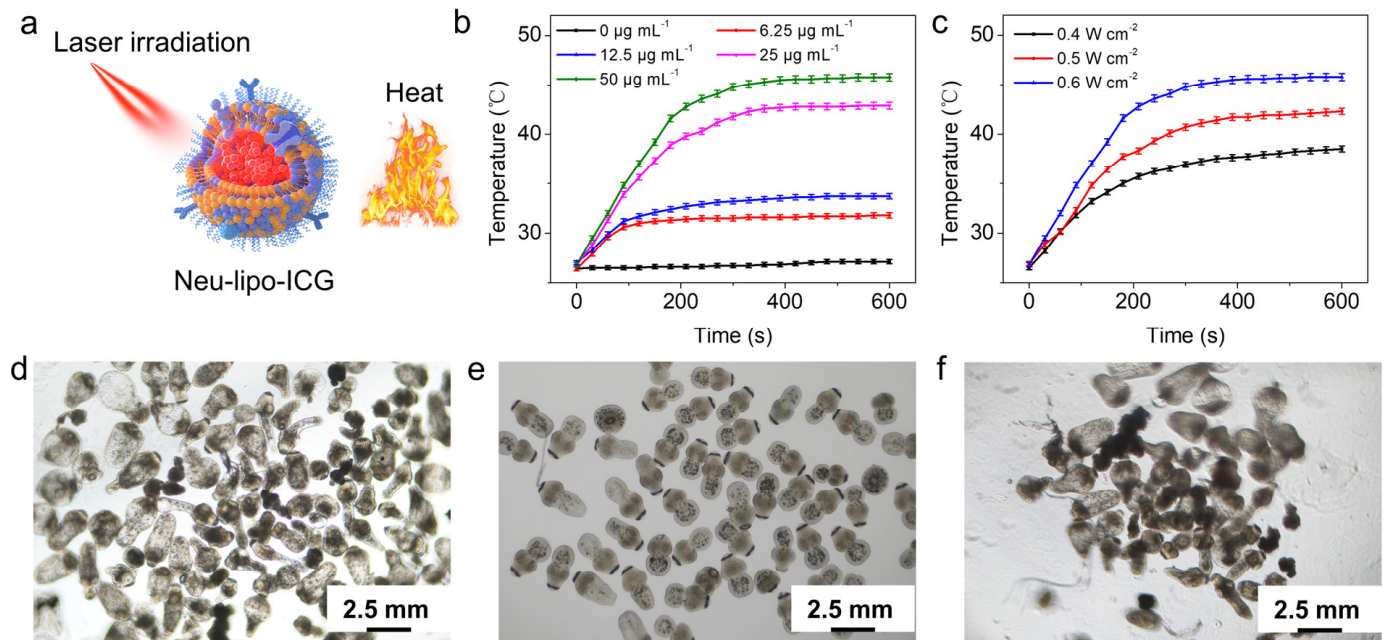


**Figure 2.** In-vitro photothermal-heating performance of Neu-lipo-ICG. (a) Schematic illustration of the photothermal therapy. (b) Photothermal-heating curves of Neu-lipo-ICG aqueous solution with different concentrations under 808 nm near-infrared laser irradiation ( $0.6 \text{ W cm}^{-2}$ ). (c) Laser irradiation density-dependant photothermal-heating curves of Neu-lipo-ICG with a concentration of  $50 \mu\text{g mL}^{-1}$ . (d) Bright-field microscope images of Neu-lipo-ICG-treated protoscolecocysts, (e) laser-treated protoscolecocysts, and (f) Neu-lipo-ICG-laser-treated protoscolecocysts.

### 3.3. In-Vivo Biocompatibility of Neu-Lipo-ICG

Neu-lipo-ICG was prepared using the U.S. Food and Drug Administration-approved biomaterials (ICG, DSPE-PEG<sub>2000</sub> and DOPC) with high biocompatibility. There was no evidence that Neu-lipo-ICG was not toxic in vivo. Thus, prior to in-vivo imaging, the toxicity of Neu-lipo-ICG was investigated to assess its biosafety for potential applications in clinics. Significantly, no evident changes in the blood indexes between the physiological saline-treated group (control) and Neu-lipo-ICG-treated group (low dose:  $0.5 \text{ mg Kg}^{-1}$  ICG, high dose:  $2.0 \text{ mg Kg}^{-1}$  ICG) were detected 24 h post-injection treatment (Figure 3a–i). Moreover, the results of the hematological and histological analysis of biomimetic ICG liposomes in mice are shown in Figure 3j,k. It shows that the hematological parameters of biomimetic ICG liposomes with a low dose and high dose did not change significantly compared with the control group. Meanwhile, the staining analysis of liver, spleen, lung and kidney tissues indicated no bleeding, inflammation or tissue necrosis. The results demonstrated biomimetic ICG liposomes have good biocompatibility in vivo.

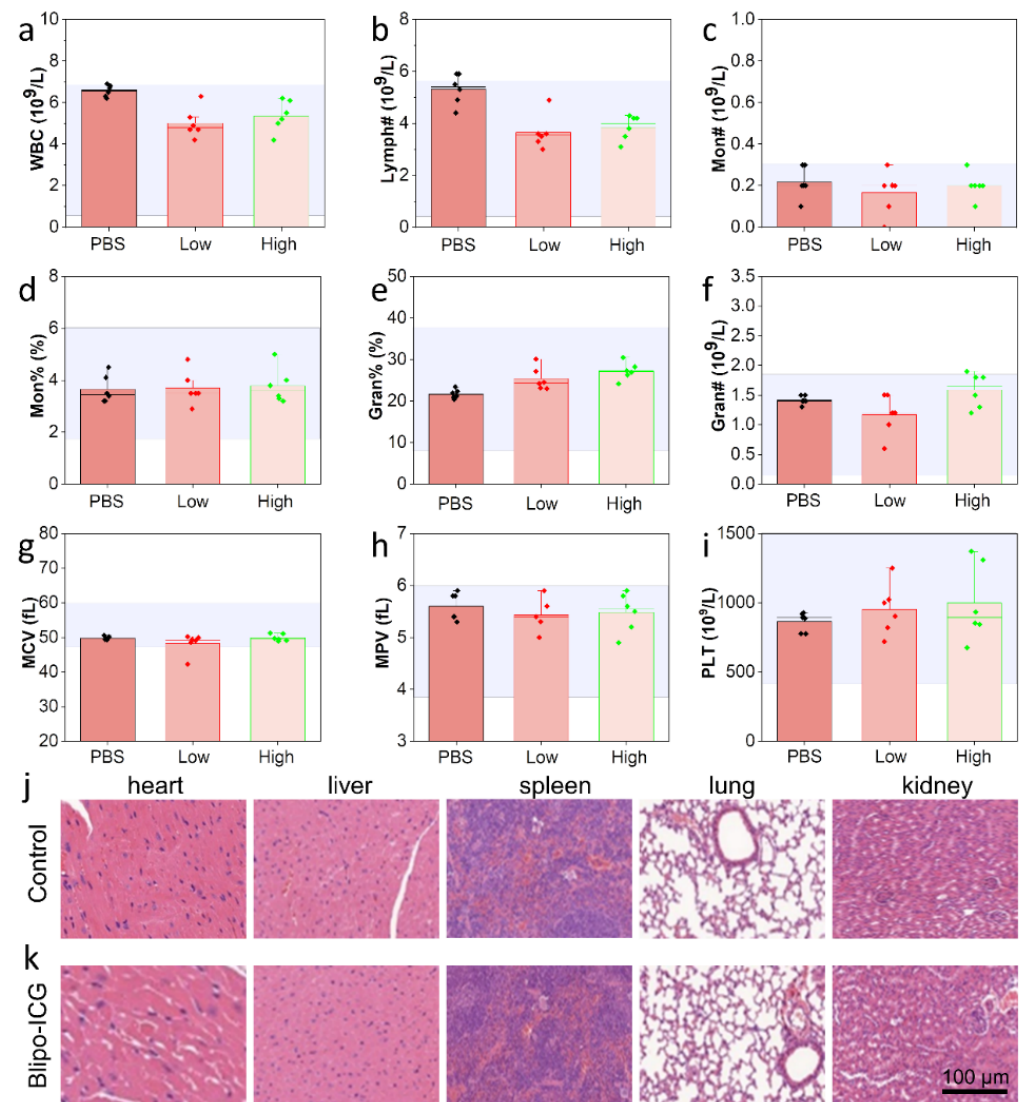


**Figure 3.** In-vivo toxicity evaluation of Neu-lipo-ICG. (a–i) Blood test parameters, including WBC (white blood cell), Lymph# (lymphocyte number), Mon# (monocyte number), Mon (monocyte), Gran (granulocytes), Gran# (granulocytes number), MCV (mean corpuscular volume), MPV (mean platelet volume) and PLT (platelet) of Balb/c mice after various treatments (n = 5, low dose: low dose:  $0.5 \text{ mg Kg}^{-1}$  ICG, high dose:  $2.0 \text{ mg Kg}^{-1}$  ICG, 24 h). (j,k) H&E stained images were acquired from the major organs (heart, liver, spleen, lung, and kidney) of physiological saline-treated and Neu-lipo-ICG-treated groups at 24 h post-injection.

### 3.4. In-Vivo Near-Infrared Fluorescence Imaging of Neu-Lipo-ICG

Subsequently, the in-vivo near-infrared fluorescence of Neu-lipo-ICG was investigated in mouse models using a highly sensitive imaging system (Figure 4a). As illustrated in Figure 4b, the fluorescence signals in liver regions were recorded after different time intervals post-injection. The sustained strong fluorescence signals in the Neu-lipo-ICG-treated group were observed over time, which were higher than that of Lipo-ICG-treated group. In comparison, the conventional Lipo-ICG-treated group showed inefficient accumulation in the liver infected tissue after 24 h post-treatment. Quantitative results further manifested that the fluorescence signal in the Neu-lipo-ICG group was 4.2-times higher than that of the Lipo-ICG-treated group 24 h post-injection (Figure 4c). These results revealed that Neu-lipo-ICG enabled an active-targeting performance in hydatid infection sites based on the inflammatory chemotaxis of neutrophil membrane proteins, and produced bright near-infrared fluorescence signals. It was noteworthy that biocompatible Neu-lipo-ICG

could be completely degraded in liver tissue after performing imaging tasks, which was beneficial for clinical translation.

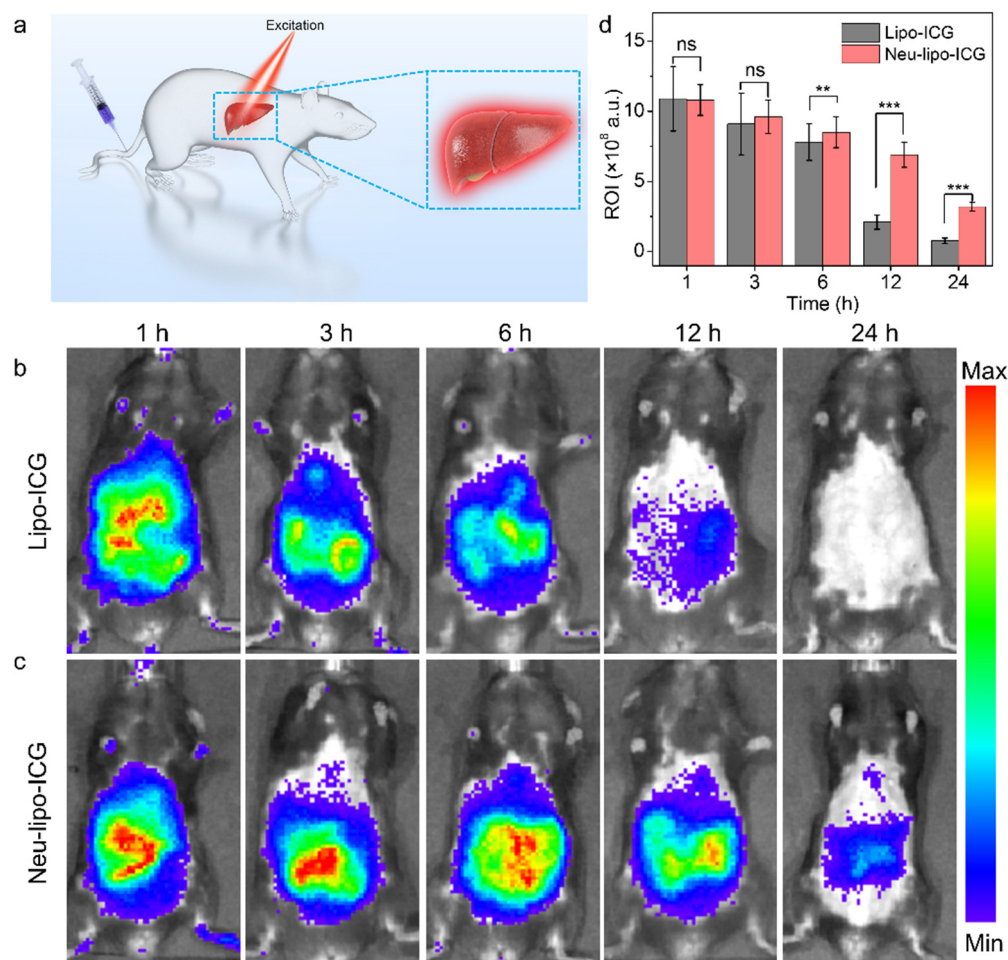


**Figure 4.** In-vivo near-infrared fluorescence imaging of Neu-lipo-ICG in mouse models infected with alveolus echinococcosis. (a) Scheme of in-vivo imaging by Neu-lipo-ICG. (b) Near-infrared fluorescence imaging of Lipo-ICG and (c) Neu-lipo-ICG at varied time points. (d) Fluorescence intensity of a region of interest (ROI) after intravenous injection of Neu-lipo-ICG ( $0.5 \text{ mg Kg}^{-1}$ ) at various time points. Statistical analysis was performed using a student's *t*-test, with \*\*\* indicating  $p < 0.005$ , \*\* indicating  $p < 0.05$ , ns indicating no significance.

### 3.5. In-Vivo Photothermal Treatment of Neu-Lipo-ICG

Encouraged by the remarkable therapeutic effect in vitro and favorable active-targeting performance of Neu-lipo-ICG in vivo, its in-vivo photothermal-treatment efficacy was investigated in mouse models (Figure 5a). Mice infected with hydatidosis were randomly divided into three groups ( $n = 5$ ), including group I: control, group II: laser irradiation, and group III: Neu-lipo-ICG + laser irradiation. The liver region was irradiated by an 808 nm laser (power density:  $0.6 \text{ W cm}^{-1}$ ) for 10 min at 24 h post-injection (dose:  $0.5 \text{ mg Kg}^{-1}$ ). The real-time temperature of the liver region was recorded by a thermal-imaging instrument during the photothermal treatment process. For mice intravenously administrated with Neu-lipo-ICG, the temperature at the liver sites rapidly increased by  $15.4 \text{ }^\circ\text{C}$  during the first 3 min and then remained at  $46.7 \text{ }^\circ\text{C}$  under near-infrared laser irradiation (Figure 5b). In comparison, the laser-irradiation-only group (group II) showed a slight temperature increase and reached  $40 \text{ }^\circ\text{C}$ , which is lower than the hyperthermia threshold ( $42.0 \text{ }^\circ\text{C}$ ), verifying its high safety. The lesion volumes in the liver tissues receiving different treatments were evaluated using ultrasound imaging and magnetic resonance imaging (Figure 5c), respectively. Neu-lipo-ICG-mediated photothermal therapy achieved significant alleviation

of the lesion volume during the detected period of 7 days, validating that Neu-lipo-ICG efficiently killed hydatids under near-infrared laser irradiation. In contrast, laser irradiation alone or Neu-lipo-ICG administration without irradiation exhibited no effect on the hydatid infect suppression. These findings confirmed that Neu-lipo-ICG could be used as a high-performance photothermal agent with excellent biocompatibility for the treatment of echinococcosis.

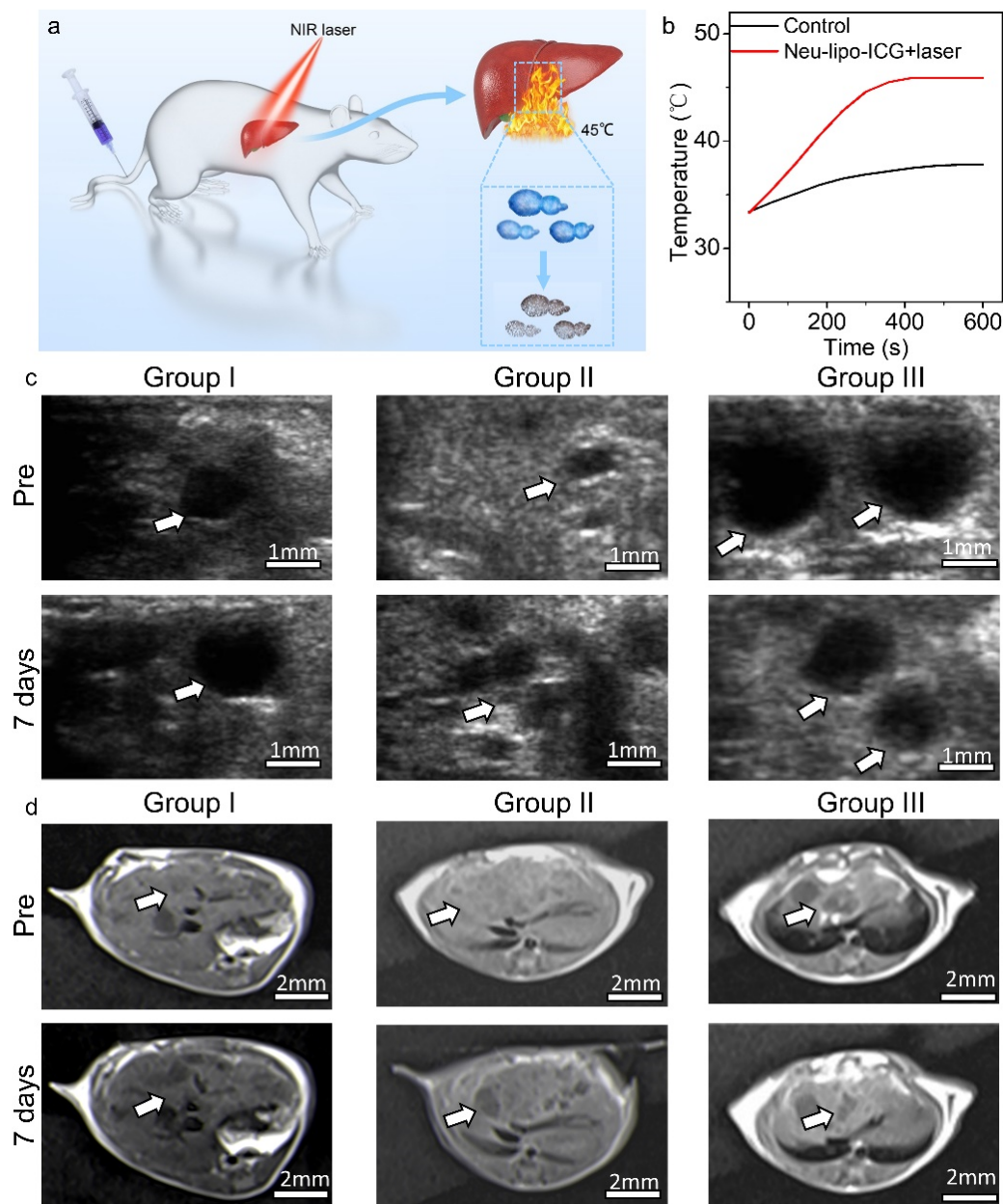


**Figure 5.** In-vivo photothermal therapy of Neu-lipo-ICG in mouse models infected with alveolus echinococcosis. (a) Scheme of in-vivo photothermal therapy by Neu-lipo-ICG. (b) Photothermal heating curves of the control group and Neu-lipo-ICG laser-treated group. (c) Ultrasound imaging and (d) magnetic resonance imaging of liver tissue of the echinococcosis-infected mice before and 7 days post-treatment.

#### 4. Conclusions

In this study, we demonstrated that Neu-lipo-ICG is the ideal phototheranostic agent for near-infrared fluorescence-imaging-guided photothermal therapy of echinococcosis. The as-obtained Neu-lipo-ICG exhibited good optical and photothermal properties. In



comparison with Lipo-ICG, the neutrophil-membrane-coating technology revealed a specific targeting ability for hydatid infected tissue through inflammatory chemotactic effects. Neu-lipo-ICG demonstrated a longer residence time in mouse models infected with alveolar echinococcosis than that of Lipo-ICG-treated group, due to its active-targeting ability. In addition, both in-vitro and in-vivo investigations manifested the Neu-lipo-ICG for the sensitive diagnosis and efficient therapy of echinococcosis in mouse models. It is noteworthy that this is the first prospective study using biomimetic liposomes for the diagnosis and treatment of zoonotic diseases, providing a promising method to explore functional nanomaterials for the rapid and efficient phototheragnostic of infectious diseases in the underdeveloped area.

**Author Contributions:** Conceptualization, W.L., Z.S. and H.Z.; methodology, X.X.; software, D.G.; validation, X.X. and J.L.; formal analysis, X.X.; investigation, J.L.; resources, X.X.; data curation, J.L.; writing—original draft preparation, Z.S.; writing—review and editing, Z.S.; visualization, H.Z.; supervision, W.L.; project administration, W.L.; funding acquisition, W.L. All authors have read and agreed to the published version of the manuscript.

**Funding:** This research was funded by the Natural Science Foundation of China (81772008).

**Institutional Review Board Statement:** The animal study protocol was approved by the Ethics committee of Xinjiang Medical University (IACUC-20140424008).

**Informed Consent Statement:** Not applicable.

**Data Availability Statement:** Not applicable.

**Acknowledgments:** This work is supported by the National Natural Science Foundation of China (81772008).

**Conflicts of Interest:** The authors declare no conflict of interest.

## References

1. Wen, H.; Vuitton, L.; Tuxun, T.; Li, J.; Vuitton, D.A.; Zhang, W.; McManus, D.P. Echinococcosis: Advances in the 21st Century. *Clin. Microbiol. Rev.* **2019**, *32*, e00075-18. [[CrossRef](#)] [[PubMed](#)]
2. Craig, P.S.; McManus, D.P.; Lightowers, M.W.; Chabalgoity, J.A.; Garcia, H.H.; Gavidia, C.M.; Gilman, R.H.; Gonzalez, A.E.; Lorca, M.; Naquira, C.; et al. Prevention and control of cystic echinococcosis. *Lancet Infect. Dis.* **2007**, *7*, 385–394. [[CrossRef](#)]
3. McManus, D.P.; Zhang, W.; Li, J.; Bartley, P.B. Echinococcosis. *Lancet* **2003**, *362*, 1295–1304. [[CrossRef](#)]
4. Craig, P.S.; Hegglin, D.; Lightowers, M.W.; Torgerson, P.R.; Wang, Q. Chapter Two—Echinococcosis: Control and Prevention. *Adv. Parasitol.* **2017**, *96*, 55–158. [[PubMed](#)]
5. Mandal, S.; Mandal, M.D. Human cystic echinococcosis: Epidemiologic, zoonotic, clinical, diagnostic and therapeutic aspects. *Asian Pac. J. Trop. Med.* **2012**, *5*, 253–260. [[CrossRef](#)]
6. Baumann, S.; Shi, R.; Liu, W.; Bao, H.; Schmidberger, J.; Kratzer, W.; Li, W.; Barth, T.F.E.; Bloehdorn, J.; Fischer, I.; et al. Worldwide literature on epidemiology of human alveolar echinococcosis: A systematic review of research published in the twenty-first century. *Infection* **2019**, *47*, 703–727. [[CrossRef](#)]
7. Gavidia, C.M.; González, A.E.; Zhang, W.; McManus, D.P.; Lopera, L.; Ninaquispe, B.; García, H.H.; Rodríguez, S.; Verastegui, M.; Calderón, C.; et al. Diagnosis of Cystic Echinococcosis, Central Peruvian Highlands. *Emerg. Infect. Dis.* **2008**, *14*, 260–266. [[CrossRef](#)]
8. Liu, H.; Zhang, C.; Fan, X.; Duan, Y.; Xiao, T.; Du, G.; Fu, Y.; Liu, H.; Wen, H. Robust Phase-Retrieval-Based X-ray Tomography for Morphological Assessment of Early Hepatic Echinococcosis Infection in Rats. *PLoS ONE* **2017**, *12*, e0183396. [[CrossRef](#)]
9. Guo, H.; Liu, W.; Wang, J.; Xing, Y. Extrahepatic alveolar echinococcus on multi-slice computed tomography and magnetic resonance imaging. *Sci. Rep.* **2021**, *11*, 9409. [[CrossRef](#)]
10. Yangdan, C.-R.; Wang, C.; Zhang, L.-Q.; Ren, B.; Fan, H.-N.; Lu, M.-D. Recent advances in ultrasound in the diagnosis and evaluation of the activity of hepatic alveolar echinococcosis. *Parasitol. Res.* **2021**, *120*, 3077–3082. [[CrossRef](#)]
11. Zhou, T.; Xu, Y.; Gong, Y.; Yu, M.; Xu, E.; Aimaiti, W.; Ma, R.; Xing, L.; Wen, H.; Wang, J.; et al. Breaking-then-curing strategy for efficient cystic echinococcosis therapy. *Chin. Chem. Lett.* **2022**, 1001–8417. [[CrossRef](#)]
12. Hillenbrand, A.; Beck, A.; Kratzer, W.; Graeter, T.; Barth, T.F.E.; Schmidberger, J.; Möller, P.; Henne-Bruns, D.; Gruener, B. Impact of affected lymph nodes on long-term outcome after surgical therapy of alveolar echinococcosis. *Langenbeck's Arch. Surg.* **2018**, *403*, 655–662. [[CrossRef](#)] [[PubMed](#)]
13. Chen, K.-F.; Tang, Y.-Y.; Wang, R.; Fang, D.; Chen, J.-H.; Zeng, Y.; Li, B.; Wen, T.-F.; Wang, W.-T.; Wu, H.; et al. The Choose of Different Surgical Therapies of Hepatic Alveolar Echinococcosis: A Single-Center Retrospective Case-Control Study. *Medicine* **2018**, *97*, e0033. [[CrossRef](#)] [[PubMed](#)]

14. Wang, H.; Li, R.; Chen, X.; Duan, B.; Xiong, L.; Yang, X.; Fan, H.; Ni, D. Remote Intelligent Assisted Diagnosis System for Hepatic Echinococcosis. In Proceedings of the Medical Ultrasound, and Preterm, Perinatal and Paediatric Image Analysis, Lima, Peru, 4–8 October 2020; pp. 3–12.
15. Zheng, X.; Wu, G.; Lv, G.; Yin, L.; Luo, B.; Lv, X.; Chen, C. Combining derivative Raman with autofluorescence to improve the diagnosis performance of echinococcosis. *Spectrochim. Acta Part A Mol. Biomol. Spectrosc.* **2021**, *247*, 119083. [[CrossRef](#)] [[PubMed](#)]
16. Liu, Y.; Bhattarai, P.; Dai, Z.; Chen, X. Photothermal therapy and photoacoustic imaging via nanotheranostics in fighting cancer. *Chem. Soc. Rev.* **2019**, *48*, 2053–2108. [[CrossRef](#)]
17. Fernandes, N.; Rodrigues, C.F.; Moreira, A.F.; Correia, I.J. Overview of the application of inorganic nanomaterials in cancer photothermal therapy. *Biomater. Sci.* **2020**, *8*, 2990–3020. [[CrossRef](#)]
18. Doughty, A.C.; Hoover, A.R.; Layton, E.; Murray, C.K.; Howard, E.W.; Chen, W.R. Nanomaterial Applications in Photothermal Therapy for Cancer. *Materials* **2019**, *12*, 779. [[CrossRef](#)]
19. Qing, G.; Zhao, X.; Gong, N.; Chen, J.; Li, X.; Gan, Y.; Wang, Y.; Zhang, Z.; Zhang, Y.; Guo, W.; et al. Thermo-responsive triple-function nanotransporter for efficient chemo-photothermal therapy of multidrug-resistant bacterial infection. *Nat. Commun.* **2019**, *10*, 4336. [[CrossRef](#)]
20. Zhou, J.; Jangili, P.; Son, S.; Ji, M.S.; Won, M.; Kim, J.S. Fluorescent Diagnostic Probes in Neurodegenerative Diseases. *Adv. Mater.* **2020**, *32*, 2001945. [[CrossRef](#)]
21. Zhi, D.; Yang, T.; O'Hagan, J.; Zhang, S.; Donnelly, R.F. Photothermal Therapy. *J. Control Release* **2020**, *325*, 52–71. [[CrossRef](#)]
22. Wei, W.; Zhang, X.; Zhang, S.; Wei, G.; Su, Z. Biomedical and Bioactive Engineered Nanomaterials for Targeted Tumor Photothermal Therapy: A review. *Mater. Sci. Eng. C* **2019**, *104*, 109891. [[CrossRef](#)] [[PubMed](#)]
23. Kim, J.; Kim, J.; Jeong, C.; Kim, W.J. Synergistic Nanomedicine by Combined Gene and Photothermal Therapy. *Adv. Drug Deliv. Rev.* **2016**, *98*, 99–112. [[CrossRef](#)]
24. Xi, D.; Xu, N.; Xia, X.; Shi, C.; Li, X.; Wang, D.; Long, S.; Fan, J.; Sun, W.; Peng, X. Strong  $\pi$ - $\pi$  Stacking Stabilized Nanophotosensitizers: Improving Tumor Retention for Enhanced Therapy to Large Tumor in Mice. *Adv. Mater.* **2022**, *34*, 2102797. [[CrossRef](#)] [[PubMed](#)]
25. Zhou, X.-Q.; Xiao, M.; Ramu, V.; Hilgendorf, J.; Li, X.; Papadopoulou, P.; Siegler, M.A.; Kros, A.; Sun, W.; Bonnet, S. The Self-Assembly of a Cyclometalated Palladium Photosensitizer into Protein-Stabilized Nanorods Triggers Drug Uptake In Vitro and In Vivo. *J. Am. Chem. Soc.* **2020**, *142*, 10383–10399. [[CrossRef](#)] [[PubMed](#)]
26. Yoon, H.-J.; Lee, H.-S.; Lim, J.-Y.; Park, J.-H. Liposomal Indocyanine Green for Enhanced Photothermal Therapy. *ACS Appl. Mater. Interfaces* **2017**, *9*, 5683–5691. [[CrossRef](#)]
27. Gupta, N.; Chan, Y.-H.; Saha, S.; Liu, M.-H. Recent Development in Near-Infrared Photothermal Therapy Based on Semiconducting Polymer Dots. *ACS Appl. Polym. Mater.* **2020**, *2*, 4195–4221. [[CrossRef](#)]
28. Liang, C.; Diao, S.; Wang, C.; Gong, H.; Liu, T.; Hong, G.; Shi, X.; Dai, H.; Liu, Z. Tumor Metastasis Inhibition by Imaging-Guided Photothermal Therapy with Single-Walled Carbon Nanotubes. *Adv. Mater.* **2014**, *26*, 5646–5652. [[CrossRef](#)] [[PubMed](#)]
29. Yang, K.; Zhang, S.; Zhang, G.; Sun, X.; Lee, S.-T.; Liu, Z. Graphene in Mice: Ultrahigh In Vivo Tumor Uptake and Efficient Photothermal Therapy. *Nano Lett.* **2010**, *10*, 3318–3323. [[CrossRef](#)]
30. Huang, X.; El-Sayed, I.H.; Qian, W.; El-Sayed, M.A. Cancer Cell Imaging and Photothermal Therapy in the Near-Infrared Region by Using Gold Nanorods. *J. Am. Chem. Soc.* **2006**, *128*, 2115–2120. [[CrossRef](#)]
31. Zhao, Y.; Zhang, Z.; Pan, Z.; Liu, Y. Advanced bioactive nanomaterials for biomedical applications. *Exploration* **2021**, *1*, 20210089. [[CrossRef](#)]
32. Sheng, Z.; Hu, D.; Zheng, M.; Zhao, P.; Liu, H.; Gao, D.; Gong, P.; Gao, G.; Zhang, P.; Ma, Y.; et al. Smart Human Serum Albumin-Indocyanine Green Nanoparticles Generated by Programmed Assembly for Dual-Modal Imaging-Guided Cancer Synergistic Phototherapy. *ACS Nano* **2014**, *8*, 12310–12322. [[CrossRef](#)] [[PubMed](#)]
33. Sheng, Z.; Hu, D.; Xue, M.; He, M.; Gong, P.; Cai, L. Indocyanine Green Nanoparticles for Theranostic Applications. *Nano-Micro Lett.* **2013**, *5*, 145–150. [[CrossRef](#)]
34. Hu, D.; Zhang, J.; Gao, G.; Sheng, Z.; Cui, H.; Cai, L. Indocyanine Green-Loaded Polydopamine-Reduced Graphene Oxide Nanocomposites with Amplifying Photoacoustic and Photothermal Effects for Cancer Theranostics. *Theranostics* **2016**, *6*, 1043–1052. [[CrossRef](#)] [[PubMed](#)]
35. Reinhart, M.B.; Huntington, C.R.; Blair, L.J.; Heniford, B.T.; Augenstein, V.A. Indocyanine Green: Historical Context, Current Applications, and Future Considerations. *Surg. Innov.* **2016**, *23*, 166–175. [[CrossRef](#)]
36. Burnier, P.; Niddam, J.; Bosc, R.; Hersant, B.; Meningaud, J.-P. Indocyanine green applications in plastic surgery: A review of the literature. *J. Plast. Reconstr. Aesthetic Surg.* **2017**, *70*, 814–827. [[CrossRef](#)]
37. Wang, H.; Li, X.; Tse, B.W.-C.; Yang, H.; Thorling, C.A.; Liu, Y.; Touraud, M.; Chouane, J.B.; Liu, X.; Roberts, M.S.; et al. Indocyanine Green-incorporating Nanoparticles for Cancer Theranostics. *Theranostics* **2018**, *8*, 1227–1242. [[CrossRef](#)]
38. Wu, M.; Zhang, H.; Tie, C.; Yan, C.; Deng, Z.; Wan, Q.; Liu, X.; Yan, F.; Zheng, H. MR Imaging Tracking of Inflammation-activatable Engineered Neutrophils for Targeted Therapy of Surgically Treated Glioma. *Nat. Commun.* **2018**, *9*, 4777. [[CrossRef](#)]